

SUPPORTING INFORMATION

**NIR-NIR Photon avalanche based luminescent thermometry
with Nd doped nanoparticles**

L. Marciniak^{1*}, A. Bednarkiewicz¹, K. Elzbieciak¹

¹Institute of Low Temperature and Structure Research, Polish Academy of Sciences, Okólna 2, 50-422 Wrocław, Poland

Properties of materials

Synthesis of materials

$\text{Y}_2\text{O}_3:\text{Nd}^{3+}$, $\text{Gd}_2\text{O}_3:\text{Nd}^{3+}$, $\text{YGdO}_3:\text{Nd}^{3+}$, $\text{YAlO}_3:\text{Nd}^{3+}$ (YAP: Nd^{3+}), $\text{Y}_3\text{Al}_5\text{O}_{12}:\text{Nd}^{3+}$ nanocrystals were synthesized using well known modified Pechinis method. Y_2O_3 (99.999 % purity from Stanfords Materials), Gd_2O_3 (99.999 % purity from Stanfords Materials), Nd_2O_3 (99.99 % purity from Stanfords Materials), $\text{AlNO}_3 \cdot 9\text{H}_2\text{O}$ (99.999% from Alfa Aesar), citric acid (99.5% purity from Avantor) and ethylene glycol ($\text{C}_2\text{H}_6\text{O}_2$ from Avantor) were used as a starting materials. Appropriate amount of oxides have been diluted in ultrapure nitric acid to produce nitrates. Afterwards aqueous solutions of nitrates have been mixed together with nonhydrate citric acid and ethylene glycol for 1 h. Next, obtained solution was heated for 1 week at 90 °C until the resin was formed. Finally fabricated resin was annealed for 16 h in air at 850 °C, temperatures. Relaying of previously obtained results, the concentration of Cr^{3+} and Nd^{3+} was fixed to 1% in respect to Y^{3+} ions, respectively¹.

$\text{LiLaP}_4\text{O}_{12}:\text{Nd}^{3+}$ nanocrystals were synthesized using coprecipitation method². Stoichiometric amounts of alkali ions carbonates (Li_2CO_3 of >99.998 % purity from Fluka Analytical,) were dissolved in deionized water. Simultaneously the lanthanum and neodymium oxides (La_2O_3 of 99.999% purity from Stanford Materials, Nd_2O_3 of 99.95% purity from Stanford Materials Corporation) were dissolved in nitric acid in order to obtain lanthanides nitrates. After mixing the water solutions of nitrates with carbonates, the obtained mixture was added to the water solution of diammonium phosphate ($(\text{NH}_4)_2\text{HPO}_4$ of >99.99 % purity from Sigma Aldrich). The solution was then dried at 90 °C for 24 h and thermally treated at 450 °C for 6h.

In case of NaYF₄:Nd³⁺ nanocrystals yttrium oxide (99,99%) and neodymium oxide (99,99%) were purchased from ALFA AESAR. Oleic acid and 1-octadecene (90%) were purchased from SIGMA ALDRICH. Acetic acid (99,5%-99,9%), ethanol (96%), n-hexane (95%), chloroform (98,5%) methanol (99,8%), ammonium fluoride (98%), sodium hydroxide (98,8%) were purchased from Avantor Performance Materials S.A. (Poland). All chemical reagents were used without further purification.

Stoichiometric amounts of lanthanide oxides (Y₂O₃, Nd₂O₃ - 1mM for a core and 1.25mM for a shell) – were mixed with 50% aqueous acetic acid. The mixture was transferred to a Teflon vessel and heated to 200°C for 120 min under pressure, with the use of stainless steel hydrothermal autoclave. The final precursor was obtained by evaporation of residual acid and water in rotatory evaporator, and further dried at 150 °C for 12h.

In a typical synthesis, 2 mM Ln³⁺ of CH₃COO₃Ln precursors, 12 cm³ of oleic acid and 30 cm³ of 1-octadecene were added to the three-neck flask. The solution was stirred and heated slowly to 140°C under vacuum atmosphere, and maintained in this temperature for 30 min to remove oxygen and water. After residual water evaporation, the nitrogen atmosphere was maintained during all synthesis process. Then, the mixture temperature was decreased to 50 °C, and solutions of ammonium fluoride (8 mM) and sodium hydroxide (5 mM) dissolved in 10 cm³ of methanol were added. Next, the obtained mixture was stirred for 30 min at 80 °C to evaporate methanol. After methanol evaporation the reaction temperature was increased quickly to 300 °C and kept at this temperature for 60 min under nitrogen atmosphere. After the NPs formation the mixture was allowed to cool to room temperature. The NPs were precipitated by the addition of ethanol and isolated by centrifugation at 10,000 rpm for 10 min. The resulting pellet was dispersed in a minimal amount of n-hexane and again precipitated with excess ethanol just for purification. After centrifugation, the NPs were dispersed in 12 cm³ of n-hexane.

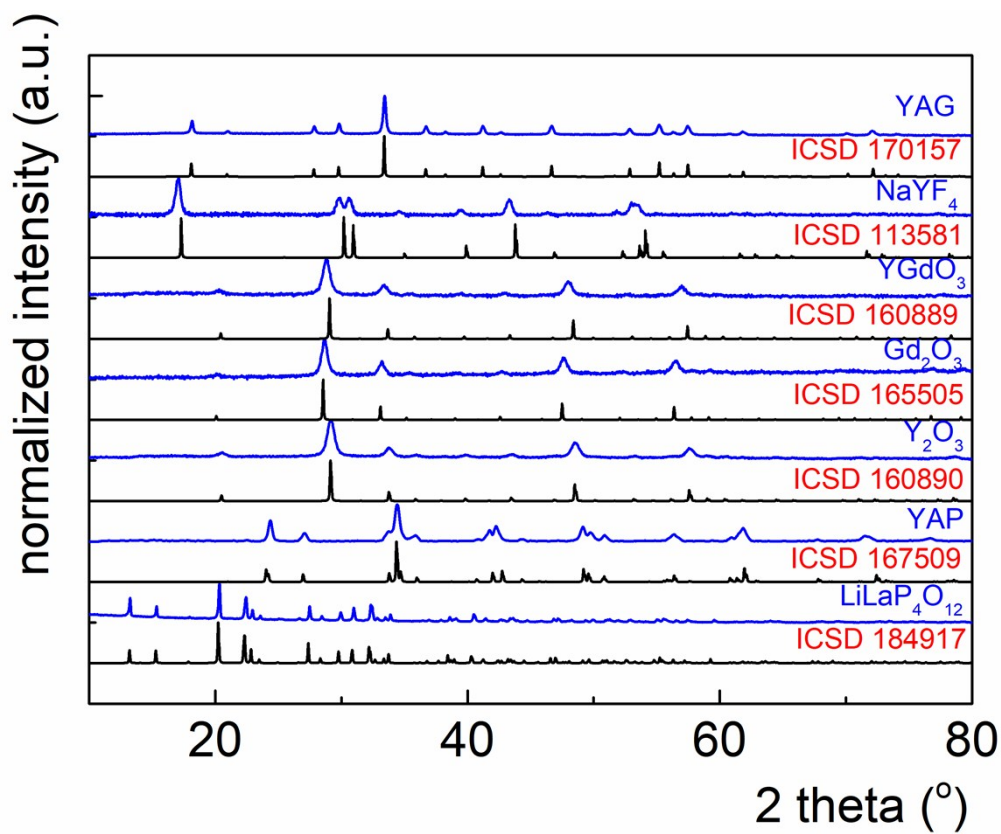


Figure S1. XRD patterns of different Nd^{3+} doped hosts

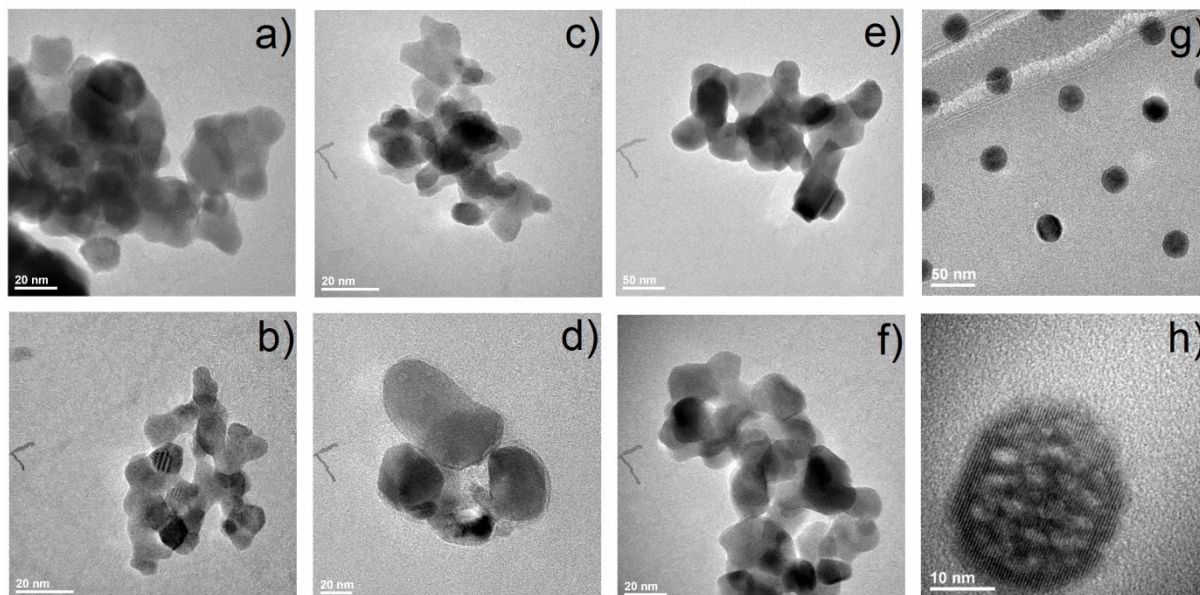


Figure S2. Comparison of TEM morphology of the studied phosphors. $\text{YAlO}_3:\text{Nd}^{3+}$ -a); $\text{Y}_2\text{O}_3:\text{Nd}^{3+}$ -b); $\text{YGdO}_3:\text{Nd}^{3+}$ -c); $\text{Gd}_2\text{O}_3:\text{Nd}^{3+}$ -d); $\text{YAG}:\text{Nd}^{3+}$ -e); $\text{LiLaP}_4\text{O}_{12}:\text{Nd}^{3+}$ -f); $\text{NaYF}_4:\text{Nd}^{3+}$ -g) and h).

Spectroscopic properties

Luminescent properties of inorganic phosphors doped with lanthanide ions are, among others, determined by the crystal field strength and point symmetry of substituted crystallographic site of host material. Therefore analyzed phosphor materials were used taking into account different crystal field strength manifested as strength of the ${}^4I_{9/2}$ and ${}^4I_{11/2}$ states splitting. Emission spectra (limited to the band of ${}^4F_{3/2} \rightarrow {}^4I_{9/2}$ transition) of different Nd^{3+} doped host phosphor are presented in Fig. S3. At higher temperatures also ${}^4F_{5/2} \rightarrow {}^4I_{9/2}$ emission band centered at 810 nm can be also observed. The emission intensity upon NRE ($\lambda_{\text{exc}}=1064$ nm) is strongly dependent on the population of ${}^4I_{11/2}$ state therefore emission intensity of described phosphor below 220 K was not observed. According to the Boltzmann population Y_1 component of ${}^4I_{11/2}$ state increases exponentially with temperature therefore as it can be observed in the representative emission spectra presented in Fig. 2a above 0°C intensity of ${}^4F_{3/2} \rightarrow {}^4I_{9/2}$ emission band rapidly increases. In order to detail analysis of the influence of host material on the thermal dependence of emission intensity upon NRE was investigated for each of synthesized phosphors and thermal evolution of Δ is presented in Fig. 2b. As it can be noticed for most of phosphors (except YAG and YAP) no emission was observed below 273 K. Above this temperature emission intensity (upon constant excitation density 900 mW/cm^2) rapidly increases even by 6 orders of magnitude up to the 573 K in case of $\text{LiLaP}_4\text{O}_{12}:\text{Nd}^{3+}$ nanocrystals. Obtained results can be well fitted using eq. 4 (solid lines in the Figure 2b)

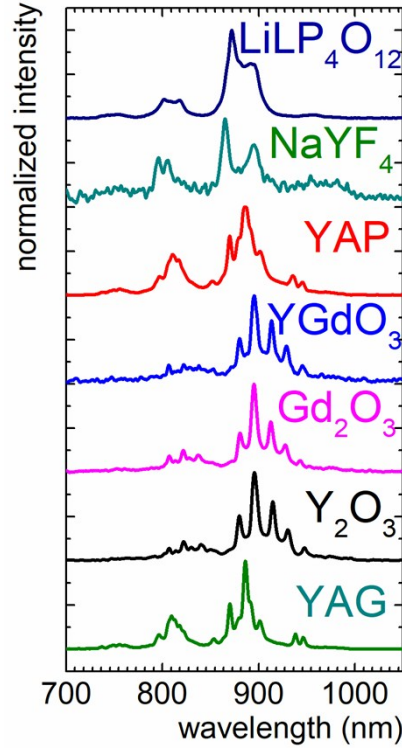


Figure S3. Comparison of emission spectra of different Nd³⁺ doped hosts obtained upon $\lambda_{\text{exc}}=1064$ nm

Phenomenological population mechanism and model

Therefore in case of photon avalanche process for temperature sensing (PAALT) sensing of temperature can be realized by comparison of emission intensity of ${}^4F_{3/2} \rightarrow {}^4I_{9/2}$ emission band upon resonant (RE) (808 nm) and nonresonant (NRE) (1064 nm) excitation:

$$\Delta = \frac{I_{NRE}(T)}{I_{RE}(T)} \quad (1)$$

Increase of the temperature will reduce emission intensity of the resonantly excited luminescence by multiphonon according to the formula:

$$I_{RE}(T) = \frac{I_0}{1 + \exp\left(-\frac{\Delta E_1}{kT}\right)} \quad (2)$$

where I_0 , ΔE_1 and k represents initial emission intensity (at low temperature) energy difference between emitting and the next lower laying energy levels and Boltzmann constant respectively. In case of Nd³⁺ ions ΔE_1 corresponds to the energy difference between ${}^4F_{3/2}$ and ${}^4I_{15/2}$ states around 6000 cm⁻¹.

In the other hand intensity of NRE luminescence can be expressed as follows:

$$I_{NRE}(T) = \frac{I_0}{1 + \exp\left(-\frac{\Delta E_1}{kT}\right)} \cdot \frac{1}{1 + \exp\left(\frac{\Delta E_2}{kT}\right)} \quad (3)$$

Due to the fact that thermal quenching of the emission intensity process affects with the same magnitude RE and NRE emission intensities eq. 1 can be reduced as follows:

$$\Delta = \frac{I_0}{1 + \exp\left(-\frac{\Delta E_1}{kT}\right)} \quad (4)$$

Based on the thermal evolution of Δ the relative sensitivity (S) of PAALT was calculated for each of phosphor basing on the following equation:

$$S = \frac{1}{\Delta} \frac{\delta\Delta}{\delta T} \cdot 100\% \quad (5)$$

where $\delta\Delta$ represents change of Δ for δT change of temperature, and presented in Fig 3a. As it was expected sensitivity of PAALT reaches its maximum at low temperatures and decreases with temperature. As it was presented in eq. 4 the changes of the intensity with temperature depends on the energy difference between ground ($^4I_{9/2}$) and first excited ($^4I_{11/2}$) states of Nd^{3+} ions. However as it was presented in some of the published studies The minimal energy difference between these states ΔE_{\min} (Z_5 Stark component of $^4I_{9/2}$ and Y_1 Stark component of $^4I_{11/2}$ states) instead of the maximal one (energy difference between Z_1 Stark component of $^4I_{9/2}$ and Y_1 component of $^4I_{11/2}$ state) the minimal energy separation should be take into account³. Therefore discussed phosphors were characterized taking into account energies of mentioned Stark components (Table 1). As it can be noticed the main difference between analyzed phosphors is related with the strength of the splitting of $^4I_{9/2}$ state by the crystal field given host material. The highest strength of the splitting (the biggest energy difference between Z_1 and Z_5 Stark components of $^4I_{9/2}$) can be found in case of the host with the highest symmetry – YAG (cubic structure) and with lowering of the symmetry (cubic in case of oxides, orthorhombic for YAP and monoclinic of $\text{LiLaP}_4\text{O}_{12}$ the reducing Stark splitting can be found and hence the enhancing of ΔE_{\min} is observed. According to the eq. 4 the increase of the ΔE_{\min} should lead to the increase of S what is in agreement with presented in Fig. 3b correlation. As it can be noticed sensitivity at 310 K of PAALT increases from 2.1%/K for YAG up to 8.2%/K for $\text{LiLaP}_4\text{O}_{12}$ nanocrystals.

Table S1. Energies of Z_5 (${}^4I_{9/2}$) and Y_1 (${}^4I_{11/2}$) Stark levels of Nd^{3+} ions and energy differences between Z_1 and Y_1 (ΔE) and between Z_5 and Y_1 (ΔE_{\min}) Stark levels of different host materials

Host material	Z_5	Y_1	ΔE_{\min} (cm^{-1})	ΔE (cm^{-1})	$h\nu$ (cm^{-1})	Ref
$\text{Y}_3\text{Al}_5\text{O}_{12}$ (YAG)	848	2001	1153	2001	870 ⁶	1
Y_2O_3	640	1899	1259	1899	590 ⁷	4
Gd_2O_3	610	1900	1290	1900	580 ⁷	4
YGdO_3	580	1910	1330	1910	590 ⁸	8
YAlO_3 (YAP)	671	2023	1352	2023	680 ⁹	9
$\text{LiLaP}_4\text{O}_{12}$	326	1939	1613	1939	1240 ¹⁰	2

Photon avalanche process is characterized by threshold dependence on excitation power. Therefore for the PAALT of the highest sensitivity ($\text{LiLaP}_4\text{O}_{12}$) the power dependence of emission intensity studies were performed at different temperatures. At low temperature (10°C) the evident threshold power (P_{th}) around 0.7 W can be found after exceeding which the emission intensity rapidly increases by one order of magnitude. No saturation of the emission intensity was observed at given excitation power range (up to 2.5 W). The increase of temperature results in the lowering of P_{th} values and the correlation of P_{th} with temperature is presented in Fig. 3f. It can be found that at 300°C the P_{th} can be found as small as 0.06 W. This dependence is a clear evidence that obtained NRE emission of Nd^{3+} ions is obtained via photon avalanche process.

Emission branching ratio

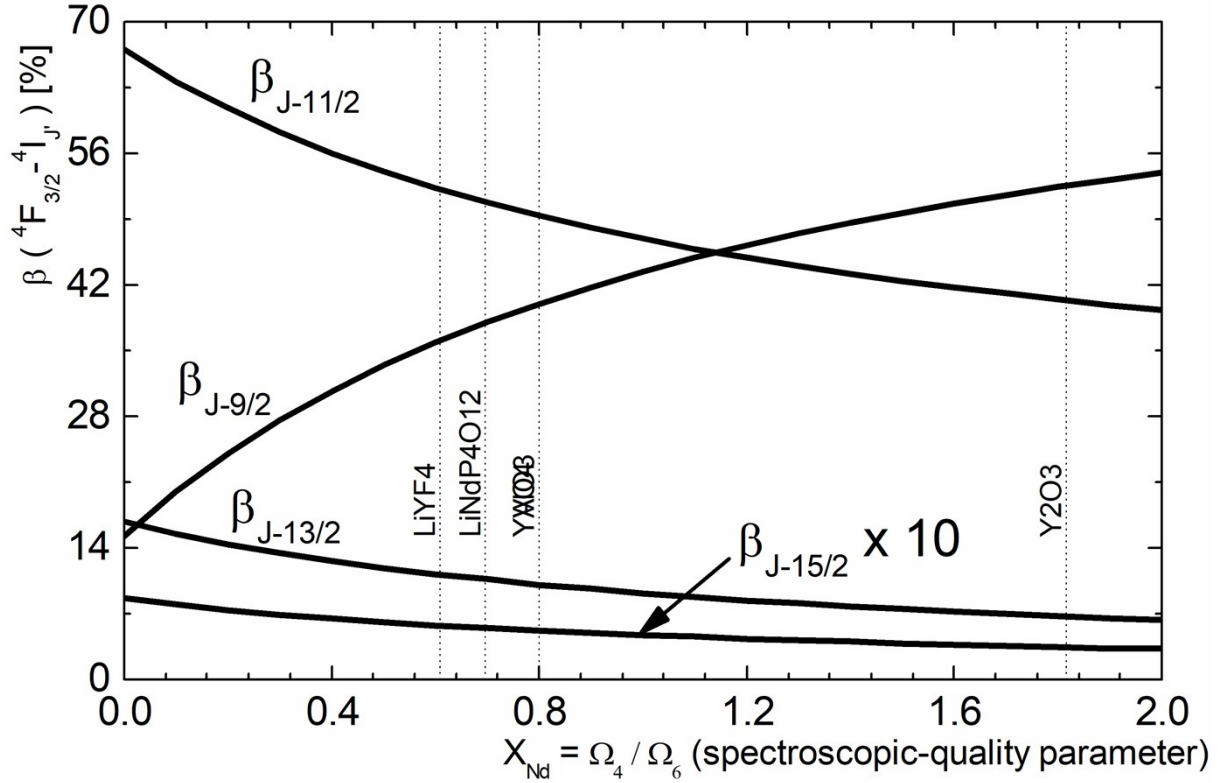


Figure S4. The theoretical emission branching ratio as a function of spectroscopic Nd parameter $X_{Nd} = \Omega_4 / \Omega_6$.

Following W. Lientz et al.⁵ one may estimate the emission branching ratio $\beta_{JJ'} = I(^4F_{3/2} \rightarrow ^4I_{J'}) / \beta_{J'} I(^4F_{3/2} \rightarrow ^4I_{J'})$, where $J' = 15/2, 13/2, 11/2, 9/2$ based on Judd-Ofelt theory as

$$\beta_{JJ'}(X_{Nd}) = \frac{(a_{J'} \cdot X_{Nd} + b_{J'}) \cdot \lambda_{JJ'}^{-3}}{\sum_{J'} (a_{J'} \cdot X_{Nd} + b_{J'}) \cdot \lambda_{JJ'}^{-3}} \quad (6)$$

Where $a_{J'}$ and $b_{J'}$ are constants equal to the squared matrix elements of the irreducible tensor operators of rank 4 and 6

$$a_{J'} = |\langle ^4F_{3/2} \| U^{(4)} \| ^4I_{J'} \rangle|^2 \quad (7)$$

$$b_{J'} = |\langle ^4F_{3/2} \| U^{(6)} \| ^4I_{J'} \rangle|^2 \quad (8)$$

And the spectroscopic parameter of Nd^{3+} - X_{Nd} is defined as the ratio between phenomenological Ω_4 to Ω_6 Judd-Ofelt parameter. Figure S5 presents the emission branching ratio versus X_{Nd} , where vertical lines indicate $\beta_{JJ'}$ values for different hosts. The $\beta_{JJ'}$ is

important in our discussion, because it determines the effectiveness, the intermediate $^4I_{11/2}$ level is populated by radiative transitions from $^4F_{3/2}$ metastable level. This in turn determines the avalanche threshold and temperature dependent $^4F_{3/2} \rightarrow ^4I_{9/2}$ emission transients.

Avalanche modelling

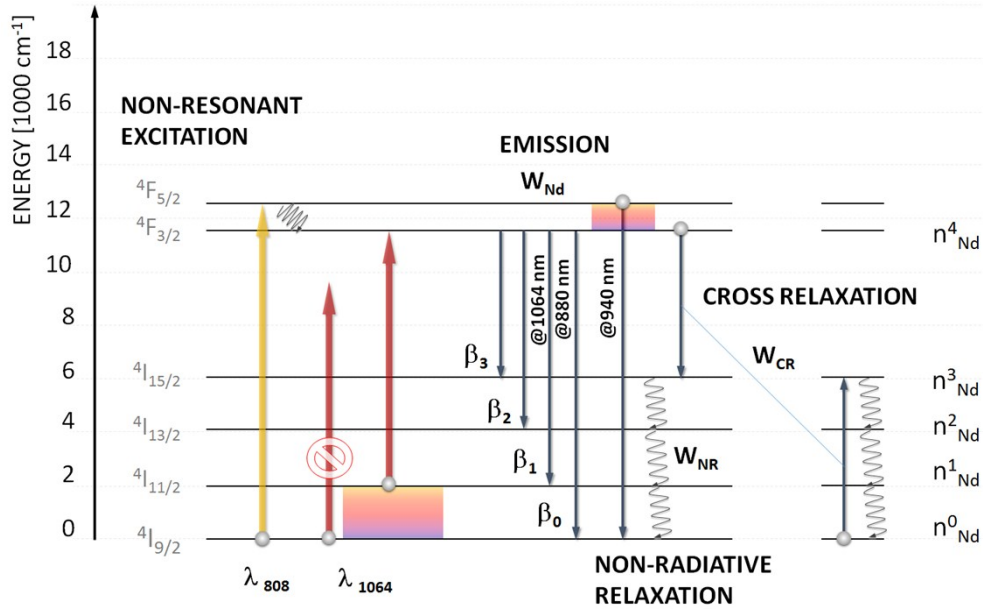


Figure S5. The energy diagram showing transitions and names respective energy levels.

$$\frac{dn_1}{dt} = W_{NR}n_1 + \beta_{9/2}W_{Nd}n_5 - n_1n_5W_{CR} - A_1n_1 \exp\left(-\frac{\Delta E_{min}}{kT}\right) \quad (9)$$

$$\frac{dn_2}{dt} = W_{NR}n_3 + \beta_{11/2}W_{Nd}n_5 - W_{NR}n_1 - P_{exc}\delta_{15}n_1 + A_1n_1 \exp\left(-\frac{\Delta E_{min}}{kT}\right) \quad (10)$$

$$\frac{dn_4}{dt} = 2W_{CR}n_1n_5 - W_{NR}n_4 + \beta_{15/2}W_{Nd}n_5 - W_{NR}n_1 \quad (11)$$

We have been numerically solving the rate equation model, by setting the phenomenological parameters:

1. rate of non-radiative transitions (W_{NR}) – this parameter is actually characteristic for a given host material and proportional to energy gap and available phonons in the matrix

2. rate of cross-relaxation (W_{CR}) – this parameter is proportional to the concentration of Nd^{3+} ions
3. variable intensity of photoexcitation (I_{EXC}),
4. photoexcitation pulse width (s) – setting reasonably long photoexcitation pulse, enables to find the steady-state intensity
5. energy gap ($\Delta E = 1600 \text{ cm}^{-1}$) – this energy gap is energy difference between highest Stark level of the ground $^4I_{9/2}$ state and lowest stark level of the $^4I_{11/2}$ level.
6. variable temperature (T, from 0 to 600 °C). Below 0°C, both theoretically and experimentally the emission was negligibly small.

First, the transients were calculated for n_0 to n_4 levels. To evaluate steady-state emission intensity, the photoexcitation pulse was fixed long enough to get saturation in transient of the population n_4 , i.e.

$$I(T) \sim n_4 = \text{fun}(I_{EXC}, W_{NR}, W_{CR}, \Delta E, T, t_{PULSE}, t).$$

Power dependent transients - modelling

Figure S6-S8 presents power dependent behavior of the system. In successive columns in the first row, the figure presents the emission power dependence $I(T) \sim n_4 = \text{fun}(I_{EXC}, W_{NR}=10^5 \text{ s}^{-1}, W_{CR}=10^5 \text{ s}^{-1}, \Delta E=1600 \text{ cm}^{-1}, T=[10,50,100,150,200^\circ\text{C}], t_{PULSE}=3 \text{ ms}, t=[0-3\text{ms}])$. The second row demonstrates the steady state emission intensity at time $t = t_{PULSE}$ versus rising excitation intensity. The third row indicated the slope factor of the power dependence. The respective colors of curves presented at first row correspond to colors of excitation intensities at second row.

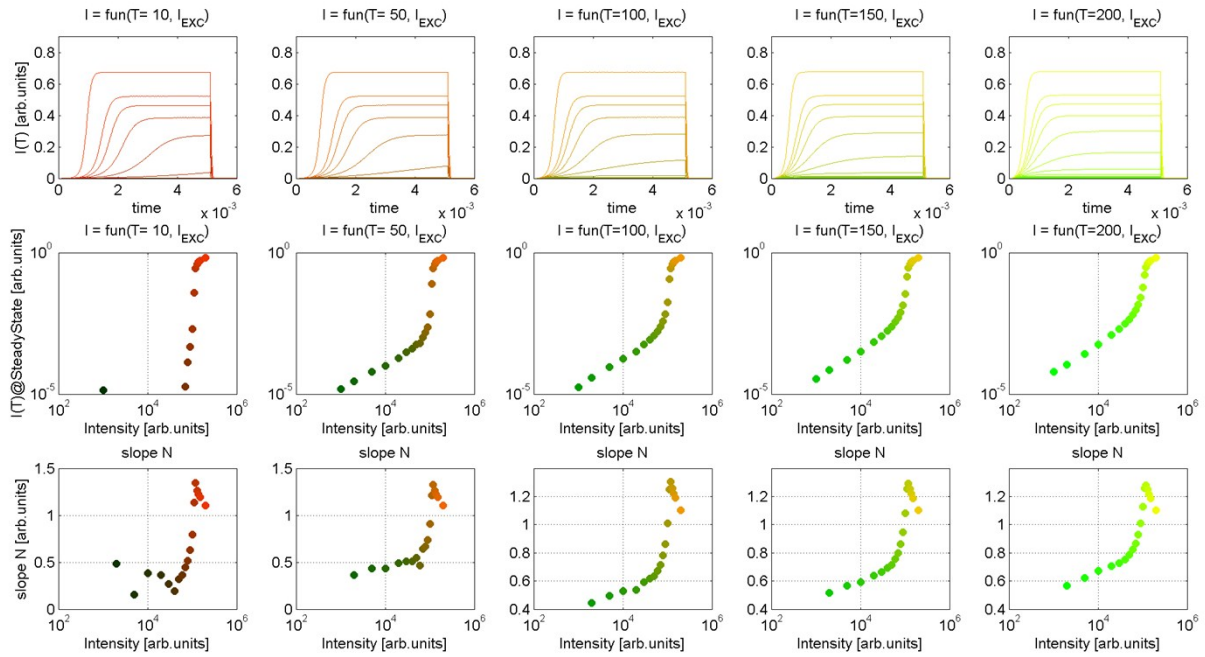


Figure S6. Power dependent behavior of the system – the role of temperature. Transients of n_4 level (1st row), steady-state emission intensity (2nd row) and power dependence slope factor N (3rd row) for different (10,50,100, 150 and 200 °C). The N was calculated as $\ln(1 \text{e}6 \Delta I_{\text{OUT}}) / \ln(\Delta I_{\text{IN}})$ between subsequent points from power dependence (row 2).

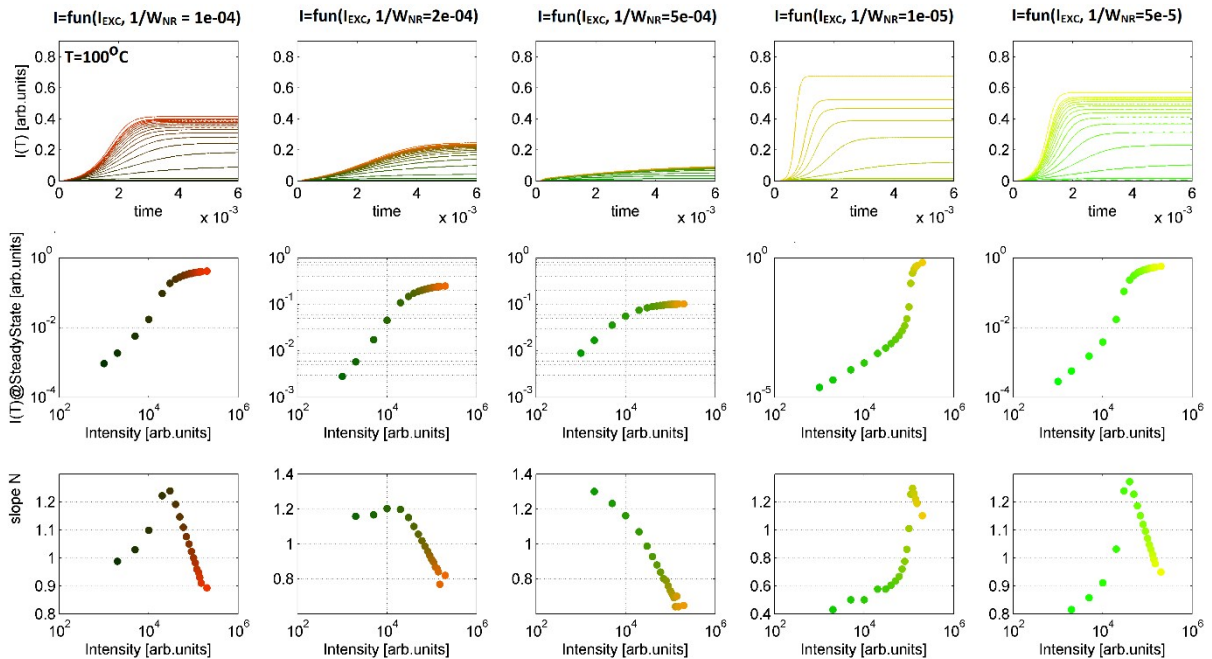


Figure S7. Power dependent behavior of the system – the role of non-radiative processes.

Transients of n_4 level (1st row), steady-state emission intensity (2nd row) and power dependent slope factor N (3rd row) for different non-radiative rates $1/W_{NR} = 1/W_{CR} = 1e-4, 2e-4, 5e-4, 1e-5, 5e-5$ [s].

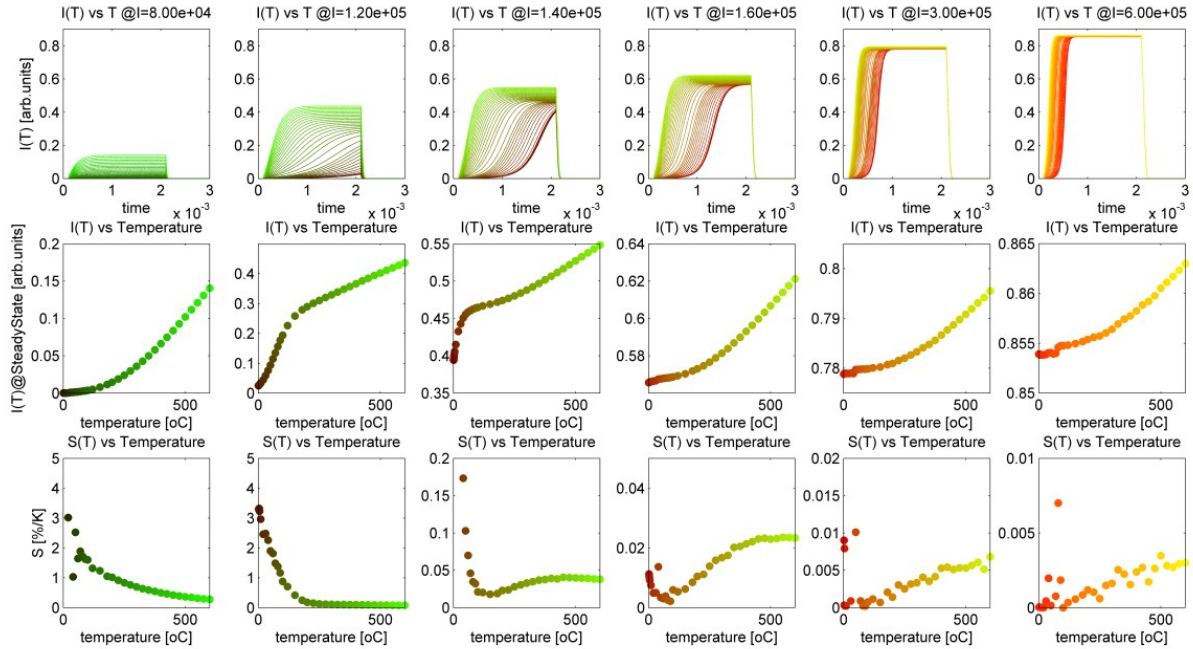


Figure S8. Temperature dependent behaviour of the system – the role of the excitation intensity.

Transients of n_4 level (1st row) over time, steady-state emission intensity (2nd row) and temperature relative sensitivity S_R (3rd row) for different intensities $I_{EXC} = (8e4, 1.2e5, 1.4e5, 1.6e5, 3e5, 6e5)$ and varying temperatures $T = (0..600^\circ\text{C})$. For the calculations $\Delta E = 1600 \text{ cm}^{-1}$ and $1/W_{NR} = 1/W_{CR} = 1e-6$ s were used.

Time resolved T determination - modelling

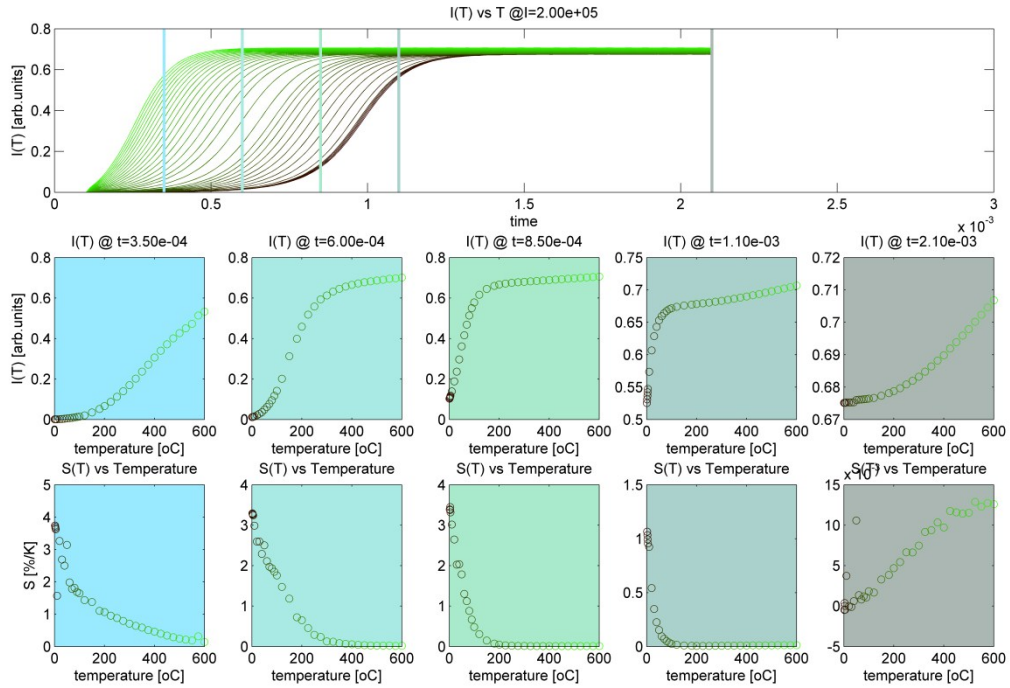


Figure S9. Temperature dependent behaviour of the system – the role of the time delayed/gated detection. In some conditions, the temperature rise is reflected in shortening the time necessary to saturate the n_4 population. Using time delayed/gated detection scheme, the delayed ($t_D=3.5e-4$, $6e-4$, $8.5e-4$, $1,1e-3$, $2.1e-3$ s after the beginning of the pulse) intensity (2nd row) and thus calculated T sensitivity (3rd row), change in different way. The figure presents transients of n_4 level (1st row) over time for rising temperature, delayed-and-gated emission intensity at t_D (2nd row) and such obtained temperature relative sensitivity S_R (3rd row). For the calculations $\Delta E=1600\text{ cm}^{-1}$ and $1/W_{NR}=1/W_{CR}=1e-6$ s were used.

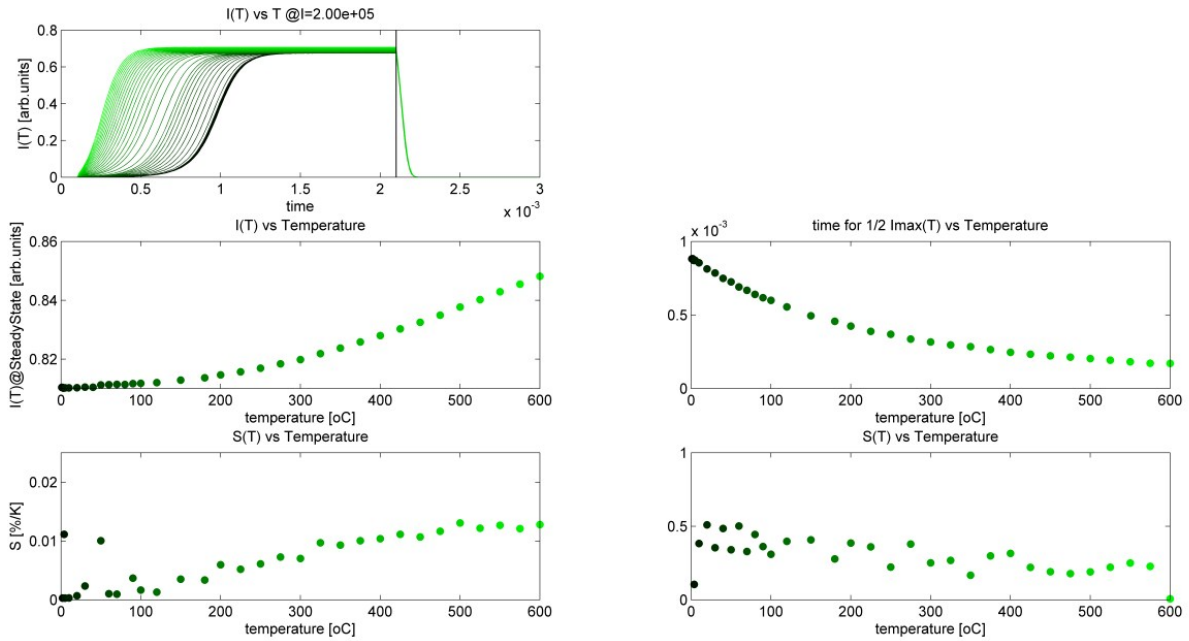


Figure S10. Temperature dependent behaviour of the system – comparison of different methods to calculate temperature sensitivity. (a) n_4 transients versus rising temperature, (b)-(e) Comparison of T readout with (b)-(c) steady-state intensity and sensitivity, (d)-(e) measuring time $\tau_{1/2}$ necessary to reach $1/2$ of maximum intensity ($I(\tau_{1/2}) = 1/2 I(t \rightarrow \infty)$).

It is important to mention the obtained sensitivity is ~ 0.5 %/K over large temperature range. If the sensitivity stay flat over such broad temperature range, the change of temperature by 1 K, would always lead to change of the figure of merit ($FOM = \tau_{1/2}$) by 0.5%, thus no special calibration of the $FOM = \text{fun}(T)$ would be necessary, and such thermometer shall behave as a primary thermometer.

Interaction of 1064 nm with tissue - safety issues

The 1064 nm laser line is probably one of the most safe one for human skin:

- no endogenous chromophores absorb this wavelength (e.g. DNA, collagen, elastin, proteins etc.) which means no photo damage to this organic molecules occurs
- also water absorption has (despite being quite substantial in NIR) a local minimum at this wavelength, and as it was shown recently this wavelength was successfully used to image Tm^{3+} doped nanoparticles through the brain tissue with no signs of brain damage¹¹. Anyway, 1064 nm should, depending on laser intensity, exhibit thermal effects only, and actually such lasers are used in medicine. Because of penetrability and the fact it is easily absorbed by melanocytes, the 1,064-nm laser is used to treat melanocytic nevi, hyperpigmentation, and other skin disorders. It is also used to treat

skin aging by stimulating dermal regeneration. Long-pulsed 1,064-nm laser is used to treat wrinkles. Q-switched laser is used in removing unwanted hair, tattoos, and pigmented and vascular lesions¹².

- two-photon imaging of living cells is performed routinely under confocal microscope, where excitation wavelengths from this spectral region are absorbed (by 2-photon mechanism) by organic chromophores which exhibit anti-Stokes emission

The key parameter here is the excitation irradiance (power density) D [W/cm^2], defined as excitation intensity P [W] focused at a given surface S [cm^2]. During our experiments, laser power used $P < 4 \text{ W}$ was focused into a small spot $\sim 2 \text{ mm}$ diameter, thus $S = 0.0314 \text{ cm}^2$, thus maximal irradiance was lower than $D_{\text{MAX}} = 127 \text{ W}/\text{cm}^2$, but the luminescence was observed already at around 0.5 W ($D=16 \text{ W}/\text{cm}^2$). Such value fall into low (safer) part of Thermal Interaction type of interaction of laser beam with tissues ($10\text{-}10^6 \text{ W}/\text{cm}^2$; temporal duration is from $1 \mu\text{s}$ to 1 min) ([link](#)). Considering the fact, the confocal life microscopy of cells is typically performed with $10^6 \text{ W}/\text{cm}^2$ irradiances, our approach shall be not only safe, but also, should enable 2D wide-field or raster scanned mapping.

From technical perspective, the readout capability depends on the brightness of the thermal luminescent probes, thus not only laser intensity matters, but also the concentration of NPs (usually much smaller than in our experiments), light scattering in tissues (usually small in NIR) and detection method. Concerning detection, we have used a CCD spectrophotometer, but a few order of magnitude more sensitive photomultipliers can be used, which shall facilitate signal quantification.

Therefore, despite promising features, such as bright emission, relatively low irradiance rates, technical simplicity of signal determination (low autofluorescence background under 1064 nm, luminescence kinetics as a measure), at this stage, it is impossible to unequivocally claim full safety for animal/human tissues.

References

- 1 L. Marciniak, A. Bednarkiewicz, J. Drabik, K. Trejgis, W. Strek, *Phys Chem Chem Phys* 2017, **19**, 7343-7351.
- 2 L. Marciniak, W. Strek, Y. Guyot, D. Hreniak, G. Boulon, *J Phys Chem C* 2015, **119**, 5160-5167.
- 3 L. Marciniak, W. Strek, D. Hreniak, *Chem Phys Lett* 2013, **583**.
- 4 K. L. Nash, R. C. Dennis, J. B. Gruber, D. K. Sardar, *J Appl Phys* 2009, **105**, 033102.
- 5 R. M. Macfarlane, *J Lumin* 1990, **45**, 1-5.
- 6 A. Chopelas, *Phys Chem Min* 2011, **38**, 709.

- 7 S. Satapathy, A. Ahlawat, A. Paliwal, R. Singh, M. K. Singh, P. K. Gupta, *CrystEngComm*, 2014, **16**, 2723-2731.
- 8 C. L. Tracy, M. Lang, F. Zhang, C. Trautmann, R. C. Ewing, *Phys. Rev. B*, 2015, **92**, 174101.
- 9 S. Kostić, Z. Z. Lazarević, V. Radojević, A. Milutinović, M. Romčević, N. Ž. Romčević, A. Valčić, *Mater Res Bull*, 2015, **63** 80-87.
- 10 L. Marciniak, W. Strek, Y. Guyot, D. Hreniak, G. Boulon, , *J. Phys. Chem. C*, 2015, **119**, 5160-5167.
- 11 E. S. Levy, C. A. Tajon, T. S. Bischof, P. Iafrati, A. Fernandez-Bravo, D. J. Garfield, M. Chamanzar, M. M. Maharbiz, V. S. Sohal, P. J. Schuck, B. E. Cohen and E. M. Chan, *ACS Nano*, 2016, **10**, 8423-8433.
- 12 Y. M. Zhang, J. Ruan, R. Xiao, Q. Zhang, Y. S. Huang, *Cell Biochem Biophys*. 2013, **67**, 1005-14.